Ab initio investigation of migration mechanisms in La-apatites

Tim K. Schultze,[†,‡] John P. Arnold,[‡] Steffen Grieshammer*[,†,‡,ϕ]

† Helmholtz-Institut Münster (IEK-12), Forschungszentrum Jülich GmbH, Corrensstraße 46, 48149 Münster, Germany

‡ Institute of Physical Chemistry, RWTH Aachen University, Landoltweg 2, 52056 Aachen, Germany

ϕ JARA-HPC, RWTH Aachen University and Forschungszentrum Jülich GmbH, 52056 Aachen, Germany

ABSTRACT: Lanthanum-apatite structures are promising materials for solid-state electrolytes, exceeding the oxygen ion conductivity of yttria-stabilized zirconia at intermediate temperatures. In recent years, several experimental contributions on La-apatites have been published, however, with divergent results. A comprehensive description of migration in dependence on composition is required to further optimize these materials and to predict the properties of similar structures. In this work, the compositions $La_{9.33}Si_6O_{26}$, $La_{10}Si_6O_{27}$ and $La_8B_2Si_6O_{26}$ (*B* = Mg, Ca, Sr, Ba) are investigated by means of density functional theory. Different migration paths are considered, and migration energies are obtained via climbing-image nudged elastic band calculations for both the vacancy and interstitialcy mechanism. Migration inside the highly conductive La-tunnel and in the *ab* plane between La-tunnels is taken into consideration. Among all investigated *B* doped compositions, $La_8Sr_2Si_6O_{26}$ shows a minimum in migration energy along the *c*-axis for the vacancy and interstitialcy mechanism in agreement with the experimental data. Furthermore, the results indicate that the type of migration mechanism depends on the synthesized composition, while the thermal excitation of defects plays a minor role. From our results, we infer that the activation energy of oxygen ion conductivity is mainly governed by the migration in the *ab* plane.

Keywords: solid oxide electrolyte, DFT, ab initio, apatites, interstitialcy, migration mechanism

Introduction

The possible application of solid oxide electrolytes ranges from biphasic oxygen membranes to solid oxide fuel cells and rechargeable oxide batteries.[1] The properties of these materials need to be tailored to the specific requirements of each application. However, high oxygen ion conductivity within the desired temperature region is paramount. Established electrolyte materials like yttria-stabilized zirconia (YSZ) exhibit high oxygen ion conductivity for high temperatures (approx. 1200 K), whereas for intermediate temperatures (below 900 K), lanthanum-apatite structures show higher oxygen ion conductivity.[2] The increasing interest in solid oxide electrolytes for intermediate temperature applications, e.g. in energy conversion, recommends more detailed investigation of these structures. To predict and optimize the ionic conductivities in lanthanum apatites, it is essential to understand the underlying migration mechanisms and their dependency on structure, composition and defects. Density functional theory (DFT) is one method of investigating these characteristics on an *ab initio* level by calculating the migration paths and respective migration energies.

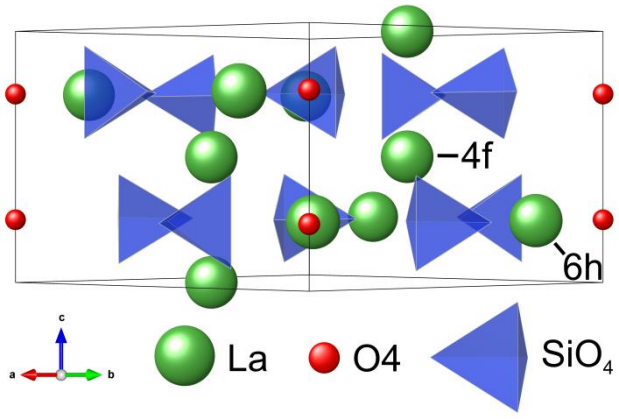

Figure 1 Lanthanum apatite structure orthogonal to the c-axis. The La 4f sites in the centre of the unit cell form pillars in *c*-axis direction, whereas the La 6h sites form a triangular coordination of O4 oxygen ions.

Lanthanum apatites crystallize in a hexagonal structure ($P6_3/m$). The structure features two Wyckoff positions for lanthanum: one that forms a triangular shape around the *c*-axis (6h) and one that forms a pillar-like structure in *c*-axis direction in the centre of the unit cell (4f), as shown in Figure 1. Adjacent triangular structural elements of the 6h sites, threefold coordinating oxygen ions (O_4), are rotated by 60° along the *c*-axis, thus appearing as a hexagonal La-tunnel (see Figure 2). The La-tunnels are separated by SiO_4 tetrahedrons in the *ab* plane. The flexibility of these tetrahedrons enables the structure to adapt to disorder and stress, and it plays a crucial role in the

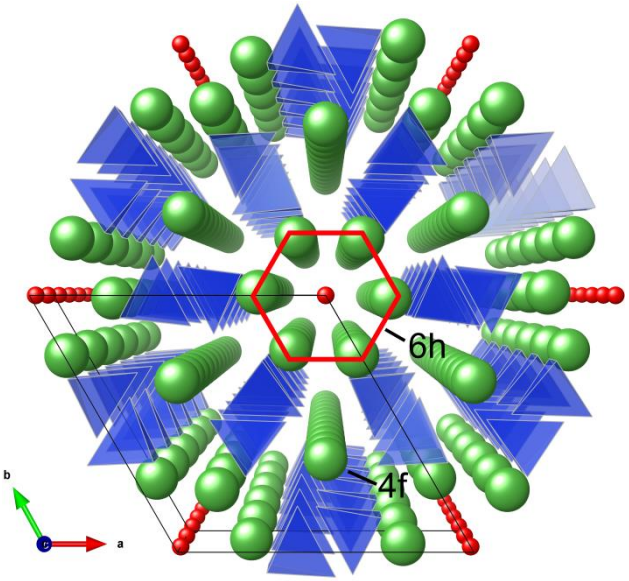

Figure 2: The hexagonal lanthanum apatite structure along the *c*-axis. The hexagonal La-tunnel highlighted red with the mobile O4 oxygen ions inside.

transport of oxygen ions.[3–5] Previous studies showed that high oxygen ion conductivity is possible along the *c*-axis, inside the hexagonal La-tunnel.[6–8] The migration of oxygen ions is accelerated in the tunnel for both the transport of vacancies and interstitials, whereby interstitial migration was found to be favoured over vacancy migration.[9–12] Measurements on single crystals as well as on polycrystalline samples showed that the conductivity in the *ab* plane is orders of magnitude lower than in the tunnels.[13–15] Starting from $La_8B_2Si_6O_{26}$ (*B* = Mg, Ca, Sr, Ba) and substituting *B* with La, the excess positive charge can either be compensated by oxygen ion interstitials, by La vacancies or by a combination of both which gives rise to a multitude of different compositions. In contrast, an excess of *B* ions could be compensated by oxygen ion vacancies.

Due to scattering of experimental data on the oxygen ion conductivity of La-apatites, several computational studies have been performed to explain the migration mechanism. Understanding the migration mechanisms on an atomic scale can provide important insight for optimizing existing compositions and predicting novel high-conductivity materials. Previous computational studies suggest different migration mechanisms and pathways using DFT and pair potential methods, almost exclusively focusing on the composition $La_{9.33}Si_6O_{26}$. In 2003, the first computational studies were performed by Tolchard *et al.*[9] Using empirical pair potentials, they proposed a "sinusoidal" interstitial mechanism with a lower energy than the vacancy mechanism.[9] In 2009, Béchade *et al.* used another set of pair potentials and found that various stable oxygen ion interstitial sites (O5) exist along the *c*-axis between the O4 sites in double-well potentials.[10] Their results indicated that the O5 interstitial moves in a "push-pull type" manner including the O4 oxygen ions, hence an interstitialcy mechanism. Using DFT, Matsunaga *et al.* showed that the interstitialcy mechanism has a significantly lower activation energy than the "sinusoidal" mechanism proposed by Tolchard *et al.*[11] Recently, Imaizumi *et al.* reported on $La_{10}Si_6O_{27}$ using DFT and kinetic Monte Carlo simulations.[12] They analysed the significance of interstitial interactions and the "getting-out" mechanism of oxygen ions leaving the La-tunnel. Both effects seem to play a substantial role for migration in the *c*-axis direction as well as in the *ab* plane. Despite the number of computational studies, there is still no detailed understanding of the relationship between composition, migration mechanisms and conductivity. To address the questions of whether the transport mechanism is a function of the oxygen ratio of the compound and how dopants affect the migration barriers, the compositions $La_{10}Si_6O_{27}$, $La_{9.33}Si_6O_{26}$ and $La_8B_2Si_6O_{26}$ were considered. Based on the results of Matsunaga *et al.*, migration barriers along the *c*-axis were calculated for both the interstitialcy and vacancy mechanisms using DFT and compared for all compositions.[11] Furthermore, defect formation energies were determined and migration between the hexagonal La-tunnels, in the *ab* plane, was examined in $La_8Sr_2Si_6O_{26}$ for comparison.

Computational details

The DFT calculations were performed with the Vienna Ab initio Simulation Package (VASP) code using the projector augmented wave (PAW) method.[16–21] For the exchange-correlation (XC) functional, the generalized-gradient approximation was adopted with the Perdew–Burke–Ernzerhof functional optimized for solids (PBEsol).[22–24] The cut-off energy for plane waves was set to 500 eV. Integration of the Brillouin zone was performed with a 2x2x2 Γ-centred k-point mesh for all considered cells. The changes of total energy and band structure energy were minimized to a threshold of 10^{-4} eV. Forces in the ionic relaxation were minimized to a threshold of 10^{-2} eV Å^{-1}.

To realize the composition $La_{9.33}Si_6O_{26}$ 1x1x3 supercells were created by tripling the unit cell in the *c* direction. Possible La sites for substitution are the 4f site as well as the 6h site; however, dopants occupy the 4f site almost exclusively, as shown by experimental data.[25–27] Therefore, the 4f site was chosen as the only site to accommodate vacancies and dopant species. For $La_{28}Si_{18}O_{78}$ the two La vacancies were arranged furthest apart to minimize energy as suggested in the literature (cf. Figure 3).[11] In the case of $La_{10}Si_6O_{27}$ an analogous $La_{30}Si_{18}O_{81}$ supercell was created to investigate different combinations of interstitial allocations. To ensure comparability, all considered, doped compositions of $La_8B_2Si_6O_{26}$ were calculated in a $La_{24}B_6Si_{18}O_{78}$ supercell structure. The dopant ions were allocated only on the two 4f sites in alternating layers in the *c*-axis direction through the supercell (cf. Figure 4). Alternative distributions of La vacancies in $La_{28}Si_{18}O_{78}$ and Sr dopant in $La_{24}Sr_6Si_{18}O_{78}$ were calculated to consider different defect environments (cf. Figure S1 and Figure S2). In the $La_{28}Si_{18}O_{78}$ supercell the La vacancies were shifted one 4f site closer towards each other. In the alter-

native $La_{24}Sr_6Si_{18}O_{78}$ supercell the distribution of Sr and La on the 4f site alternates within the layer and along the *c*-axis.

Charged supercells where realized in VASP by adjusting the number of electrons and introducing a background charge for compensation. Except for $La_{30}Si_{18}O_{81}$ all compositions where calculated as charged supercells due to the introduction of oxygen vacancies or interstitials. The effect of interaction between defects and background charge is expected to be neglectable, especially for the migration energies. The initial structures were taken from the literature and subsequently optimized using the VASP code. During the calculations, we allowed for relaxation of the ion positions, cell shape and cell volume. The transition states and migration barriers were obtained at constant volume by the climbing-image nudged elastic band (CI NEB) method.[28–32]

Results

Bulk properties

The supercells were relaxed with the conventional PBE functional and the PBE functional optimized for solids (PBEsol). A comparison of the calculated volumes versus experimental data (Table S1) shows an anticipated trend of increasing cell volume with increasing radius of the dopant on the 4f site. The volumes of $La_{9.33}Si_6O_{26}$ and $La_{10}Si_6O_{27}$ are close to that of $La_8Sr_2Si_6O_{26}$ which implies that La ion, La vacancy and Sr occupy similar space in the unit cell. Furthermore, the results from the PBEsol functional agree better with the experimental data, and thus all subsequent calculations were performed with the PBEsol functional. To estimate the finite size effect due to periodic boundaries, additional calculations in a 2x2x3 supercell were conducted. Results showed that the energy difference for stable interstitial positions in $La_{9.33}Si_6O_{26}$ was below 0.05 eV, thus all calculations were performed in the 1x1x3 supercell.

Anti-Frenkel defects were calculated for all compositions by moving one oxygen ion from an O4 site to the furthest O5 site and subsequently relaxing the structure. The resulting energies of formation are given in Table S1. The formation energies for the doped variants increase with the radius of the dopant species, which could be caused by a decrease in available cell volume for the oxygen interstitial. $La_{9.33}Si_6O_{26}$ has the lowest formation energy with 3.77 eV. It should be noted that the interaction of oppositely charged defects within the supercell is expected to stabilize the defects, and therefore the values reported here are lower bounds to the energy of formation for diluted defects. On account of the high formation energies, the number of defects due to anti-Frenkel disorder is expected to be rather low, even at elevated temperatures (cf. Table S1).

Vacancy mechanism

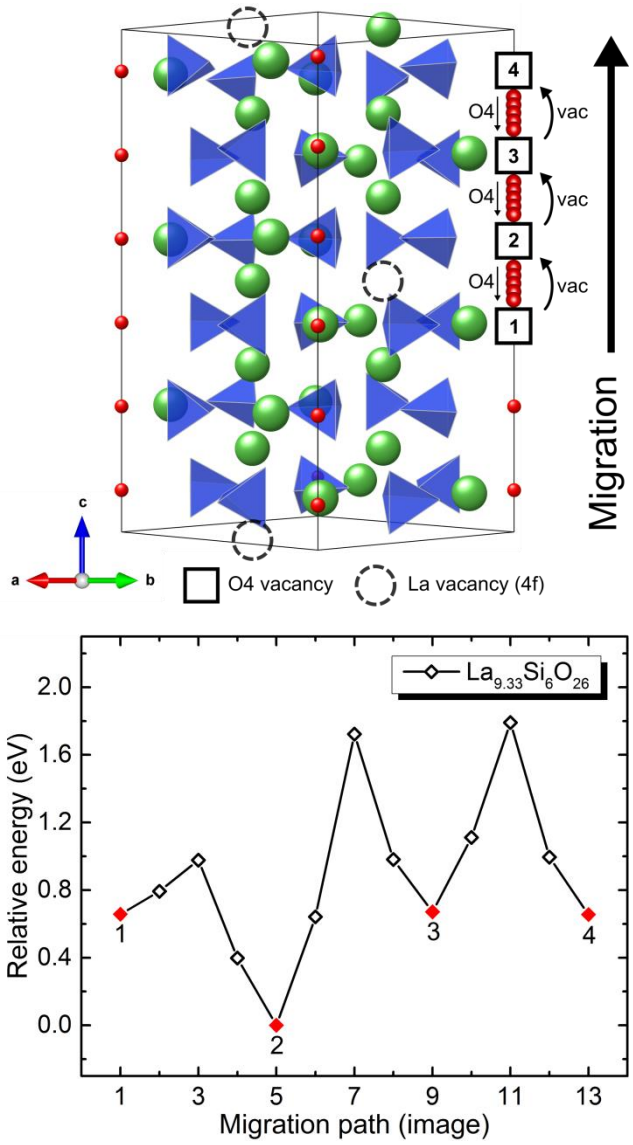

Figure 3 Migration path (top) and energy profile of vacancy migration in $La_{9.33}Si_6O_{26}$ (bottom). Top: 1x1x3 supercell orthogonal to the c-axis. The dotted spheres mark the La vacancies on 4f sites. The black squares show the O4 vacancies (vac) moving in counter motion to the O4 oxygen ions. Bottom: The solid red symbols show stable configurations of energy minima. The hollow black symbols show interpolated NEB images. The numeration of the stable configurations corresponds with those in the migration path. The oxygen vacancy passes the La vacancy between configuration 1 and 2. The line provides a guide to the eye.

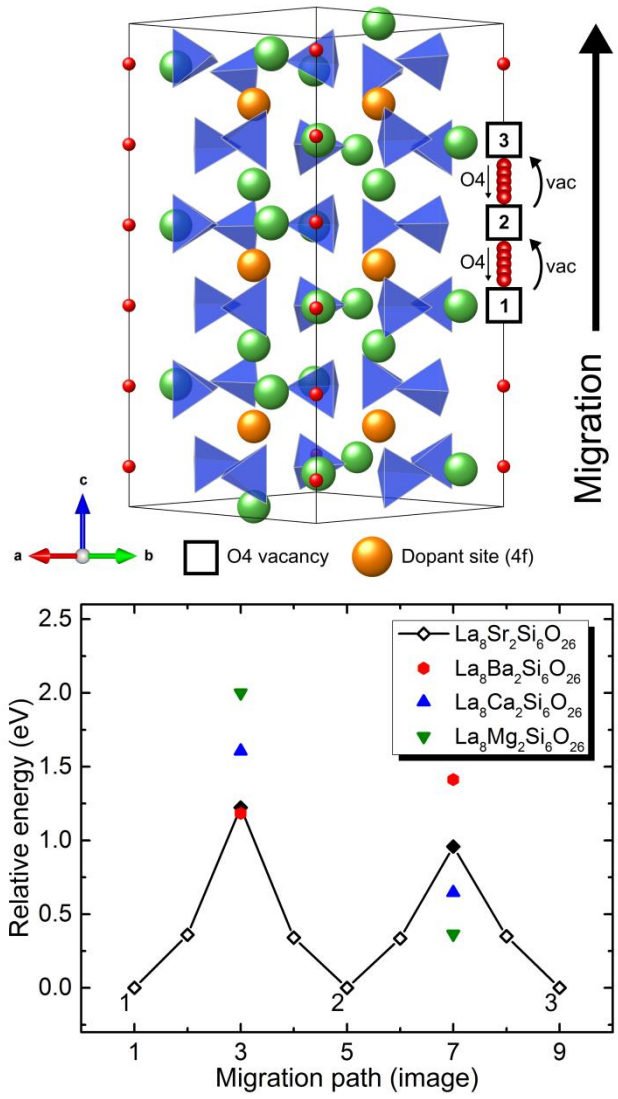

Figure 4 Migration path (top) and energy profile of the vacancy migration in $La_8B_2Si_6O_{26}$ for B = Mg, Ca, Sr, Ba (bottom). Top: 1x1x3 supercell orthogonal to the c-axis. The yellow spheres mark the dopant on 4f sites. The black squares show the O4 vacancies (vac) moving in counter motion to the O4 oxygen ions. Bottom: The solid symbols show the transition state energy of the composition found by CI NEB. The hollow black symbols show the NEB images for $La_8Sr_2Si_6O_{26}$. The numeration of the stable configurations corresponds with those in the migration path. The vacancy passes the dopant between 1 and 2. The line provides a guide to the eye.

To investigate vacancy migration, one oxygen ion was removed from an O4 site and the structure was relaxed. Subsequently, the vacancy was shifted along the *c*-axis to determine all non-equivalent, stable configurations as depicted at the top of Figure 3 and Figure 4. For $La_{9.33}Si_6O_{26}$ three non-equivalent configurations were determined and two for $La_8B_2Si_6O_{26}$ due to the positions of the La vacancies and *B* dopants. Thus, configuration 1 is equal to configuration 4 in $La_{9.33}Si_6O_{26}$ and configuration 1 is equal to configuration 3 in $La_8B_2Si_6O_{26}$. Based on these structures, CI NEB calculations were conducted to obtain the migration barriers between stable positions. The results are given in Table 1, Figure 3 and 4.[33,34]

The migration energies vary in the range of 1.22 eV to 2.00 eV with the Sr-containing structure having the smallest barrier. In the most stable configuration of $La_{9.33}Si_6O_{26}$ the oxygen vacancy occupies position 2, next to the La vacancy. The oxygen vacancy is thus trapped by the La vacancy, with a lowered migration barrier in the vicinity while the migration barrier away from the La vacancy is significantly increased. The asymmetry of the energy profile is due to distortion of the supercell caused by the La vacancies. In $La_8B_2Si_6O_{26}$ the dopant increases the migration barrier of the oxygen vacancy between configuration 1 and 2. This effect decreases with increasing dopant size with a minimum for Ba. However, the migration barrier between configuration 2 and 3 increases with the dopant radius such that $La_8Mg_2Si_6O_{26}$ shows the lowest migration barrier. The change in height of the migration barriers is caused by two effects: the interaction between the oxygen vacancy and dopant, which primarily affects the first migration barrier, and the decrease in cell volume due to the dopant size, which in turn hampers the migration of the oxygen ions moving in counter direction to the vacancy. Due to the alternating layer structure of the 4f sites in the *c* direction, the distances between the triangular La 6h formations alternate depending on the dopant influencing both migration barriers (cf. Figure S3). These effects are minimized for $La_8Sr_2Si_6O_{26}$, consequently showing the lowest overall migration energy for the vacancy mechanism.

As a lattice-distortion-free reference vacancy migration in $La_{30}Si_{18}O_{77}$ was investigated (cf. Figure S4). The supercell features no defects except for one oxygen vacancy in the La-tunnel. The calculated barrier is 1.02 eV. The difference in the migration barrier for $La_{9.33}Si_6O_{26}$ and $La_8B_2Si_6O_{26}$ can be attributed to the influence of the respective defects (cf. Table 1).

Table 1 Calculated migration barriers ΔE_{mig} for the interstitialcy and vacancy mechanism and experimental migration energies (E_A) from the literature.

Composition	ΔE_{mig} (eV) Interstitialcy (Calc.)	ΔE_{mig} (eV) Vacancy (Calc.)	E_A (eV) (Exp.)
$La_{9.33}Si_6O_{26}$	0.30	1.72	0.74
$La_8Mg_2Si_6O_{26}$	0.16	2.00	-
$La_8Ca_2Si_6O_{26}$	0.12	1.61	1.62
$La_8Sr_2Si_6O_{26}$	0.09	1.22	1.14
$La_8Ba_2Si_6O_{26}$	0.18	1.41	1.21
$La_{10}Si_6O_{27}$	0.62	-	0.64

Interstitialcy mechanism

To investigate the interstitialcy mechanism one oxygen interstitial was introduced onto an O5 site of every composition's supercell. The determined interstitial sites agree with those generally proposed by Béchade et al. for

$La_{9.33}Si_6O_{26}$ (left side of Figure 5).[10] Between two O4 ions, there are two layers of stable interstitial sites inside the La-tunnel slightly tilted away from the *c*-axis. Each layer consists of three energetically equivalent O5 interstitial positions that are rotated 120° apart, leading to a triangular layout around the *c*-axis. These triangular structures of La and O5 interstitial positions are stacked along the *c*-axis and rotated by 60° to their immediate adjacent neighbours. The migration proceeds as a combination of interstitial and interstitialcy mechanisms, as proposed by Matsunaga *et al.*[11] The migration between two O5 interstitial layers can be described by an interstitial jump, while the migration from an O5 interstitial layer to an O4 site follows an interstitialcy mechanism, where the migrating O5 ion moves to an O4 site, pushing away the O4 ion to an adjacent interstitial layer. The number of non-equivalent layers depends on the distribution of the dopant ions or lanthanum vacancies. For the structures described in Section 2, six different layers were found for $La_{9.33}Si_6O_{26}$, as depicted on the left of Figure 5 and Figure 6, while four different layers were found for the doped apatites, as depicted on the left of Figure 7 plus Figure 8.

In order to quantify the effects of the different defects a lattice-distortion-free interstitialcy migration in $La_{30}Si_{18}O_{79}$ was considered (cf. Figure S5). The regarded supercell features no defects except for one oxygen interstitial. The interstitial migration between two adjacent interstitial sites shows a 0.05 eV migration barrier whereas the interstitialcy migration via an O4 oxygen ion shows a migration barrier of 0.07 eV.

$La_{9.33}Si_6O_{26}$

Figure 5 shows the interstitialcy migration path in $La_{9.33}Si_6O_{26}$ as a superposition of all stable configurations along the migration path (right-hand side). The colours track the individual oxygen ions, while the numbers correspond to the individual configurations. Starting at configuration 1, the red oxygen ion occupying an interstitial site migrates to the position in configuration 2 by pushing the orange O4 oxygen ion to an interstitial position. As described earlier, the interstitial layers are rotated against each other; one position is rotated 180° relative to the start position of the migrating ion and two are rotated by 60° (cf. Figure S6). An oxygen ion that migrates from an O5 interstitial site to an O4 site, pushing the regular oxygen ion to an interstitial layer, has three possible sites it can occupy. One site has the same orientation as the starting position of the "pushing" O5 oxygen ion and is only shifted along the *c*-axis. Two equivalent sites are additionally rotated by 120° relative to the position of the original O5 oxygen ion. For the interstitialcy migration, the 120° rotated sites are energetically favoured. In the next step the O5 ion can jump to one of three sites in the adjacent interstitial layer. The calculations indicate that the migration barrier is minimized if the oxygen ion migrates to a 60° rotated site instead of a 180° rotated site.

Figure 6 shows the energy profile of the migration path in $La_{9.33}Si_6O_{26}$ with numeration for all stable configurations corresponding to Figure 5. In configuration 1, the

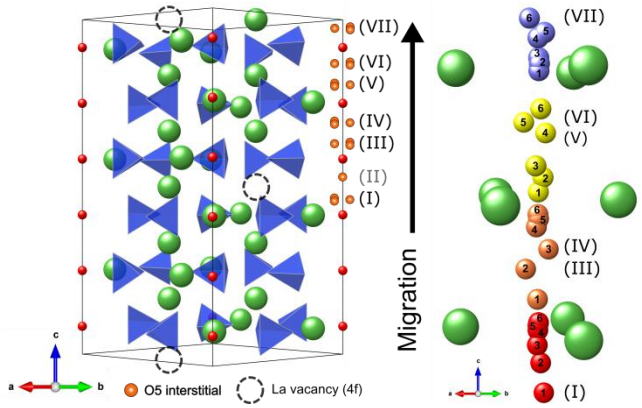

Figure 5 Left: 1x1x3 supercell of $La_{9.33}Si_6O_{26}$ orthogonal to the c-axis. The stable oxygen interstitial sites (O5), arranged in a layer structure with three equivalent positions per layer, are displayed in orange. This La vacancy distribution leads to six different O5 interstitial layers for $La_{9.33}Si_6O_{26}$. Right: Migration path of O4/O5 oxygen ions in $La_{9.33}Si_6O_{26}$ along the c-axis. Each colour tracks one oxygen ion. The numbers correspond to the configurations in Figure 6; the roman numerals correspond to the left.

interstitial occupies an O5 interstitial site in proximity to the La vacancy in layer I. Layer II does not exist in $La_{9.33}Si_6O_{26}$ due to the structural distortion induced by the La vacancy. Therefore, the interstitial migrates directly to a regular O4 oxygen site and the structure relaxes into configuration 2. The increase in energy of approximately 0.22 eV between configuration 1 and 2 may be attributed to a decrease in available space for layer III and IV compared to layer I and II due to a decrease in distance between the adjacent La 6h triangular structures by 0.5 Å (13 %). The structural distortion generated by the La vacancies results in different O4-O4 distances, which have their maximum in the vicinity of the La vacancy (cf. Fig-

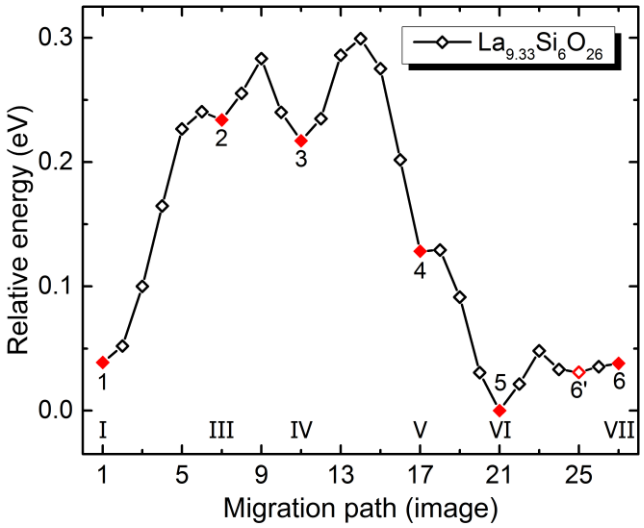

Figure 6 Energy profile of the interstitialcy migration in $La_{9.33}Si_6O_{26}$ along the *c*-axis. The solid red symbols show stable configurations. The hollow black symbols represent NEB images. The Roman numeration of the stable configurations corresponds to Figure 5. The line provides a guide to the eye.

ure S3). Between configuration 2 and 3, the O5 ion migrates from an interstitial site in layer III to an interstitial site in layer IV with a very low energy barrier of approx. 0.05 eV. From configuration 3 onwards, interstitialcy and interstitial mechanisms alternate until the O5 ion occupies an interstitial site in layer VII and the structure relaxes into configuration 6, which is equivalent to configuration 1. Configuration 6' is minimally shifted compared to 6 but also shows an energy minimum using CI NEB. However, the energy landscape between 6' and 6 is very shallow, which again can be attributed to the relative increase in available space for the O5 interstitial layers I and II, as discussed above. The total height of the migration barrier between the most stable configuration 5 and the maximum determined by CI NEB is 0.3 eV. It appears to be mainly determined by the trapping of the interstitial by the La vacancy and the unfavourable structural distortion around the O5 interstitial sites when leaving the proximity of the La vacancy.[35] This is confirmed by comparing $La_{9.33}Si_6O_{26}$ to the reference cell without lattice distortion (cf. Figure S5). While the migration barrier in the reference cell does not exceed 0.07 eV, the interstitial migration barriers as well as interstitialcy migration barriers increase drastically in the presence of La vacancies (cf. Table 1). To test the influence of the La vacancy distribution a second supercell was considered. In this alternative distribution the La vacancies are shifted closer towards each other by one 4f site, as described above (cf. Figure S1). In this structure the total height of the migration barrier decreases slightly to 0.27 eV (cf. Figure S1). This could be due to a more favourable spatial division between the layer structures even though the difference in energy is small.

$La_8B_2Si_6O_{26}$

The migration path for the earth-alkaline-doped apatites is analogous to that in the La-deficient apatite. Due to the arrangement of the dopant ions, only four non-equivalent layers are present, as described above. On the right of Figure 7, the migration path of $La_8Sr_2Si_6O_{26}$ is shown exemplarily for all doped compounds. The interstitial moves along the *c*-axis in an alternating interstitial/interstitialcy mechanism from layer I to the equivalent layer V (left site in Figure 7) comparable to $La_{9.33}Si_6O_{26}$. Figure 8 shows the corresponding energy profile of the migration. Like the vacancy mechanism, the shape of the energy profiles for the other dopants differs only quantitatively and they are therefore not shown here (cf. Figure S7). Among the investigated compounds, the Sr-doped structure shows the lowest migration barrier with an energy of 0.09 eV, as given in Table 1. Apart from the difference in radius, the available space for the O5 interstitial sites, the O4-O4 distances and the interaction between migrating oxygen ion and dopant or vacancy also appear to have an influence due to the larger migration barrier in $La_{9.33}Si_6O_{26}$ (cf. Figure S3). These characteristics lead to different trapping qualities of the defects. In Figure 8, a different behaviour can be observed for the doped apatites than for $La_{9.33}Si_6O_{26}$ (Figure 6). In the vicinity of the dopant (configuration 1 and 2; layer I and II; Figure 8), the migration barrier is low, but increases drastically when the oxygen ion leaves the proximity of the dopant (configuration 2→3). In addition, the migration barrier for the migration away from layer III and IV is increased compared to layer I and II and consequently the oxygen ion is trapped by the La ions. This supposition is supported by comparing $La_8B_2Si_6O_{26}$ to the reference cell without lattice distortion (cf. Figure S5). The difference in migration barrier of $La_8B_2Si_6O_{26}$ and the reference cell (0.07 eV) can be attributed to the respective dopant (cf. Table 1). To test the influence of the dopant distribution a second supercell was considered for $La_8Sr_2Si_6O_{26}$. As described earlier the distribution of Sr and La on the 4f sites alternates within the layer and along the *c*-axis showing a more homogeneous distribution (cf. Figure S2). The total height of the migration barrier decreases to 0.07 eV (cf. Figure S2). By creating an invariant environment during migration, the individual migration barriers give information about the energy difference between interstitial and interstitialcy migration mechanism which is 0.03 eV. As in $La_{9.33}Si_6O_{26}$ the energy difference between the two defect distributions is small.

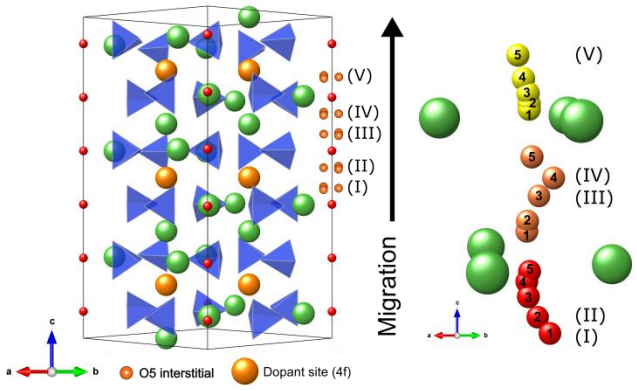

Figure 7 Left: 1x1x3 supercells of $La_8B_2Si_6O_{26}$ orthogonal to the *c*-axis. The stable oxygen interstitial sites (O5), arranged in a layer structure with three equivalent positions per layer, are displayed in orange. The allocation of the dopants leads to four different interstitial layers. Right: Migration path of O4/O5 oxygen ions in $La_8Sr_2Si_6O_{26}$ along the *c*-axis. Each colour tracks one oxygen ion. The numbers correspond to the conformations in Figure 8; the roman numerals correspond to the left.

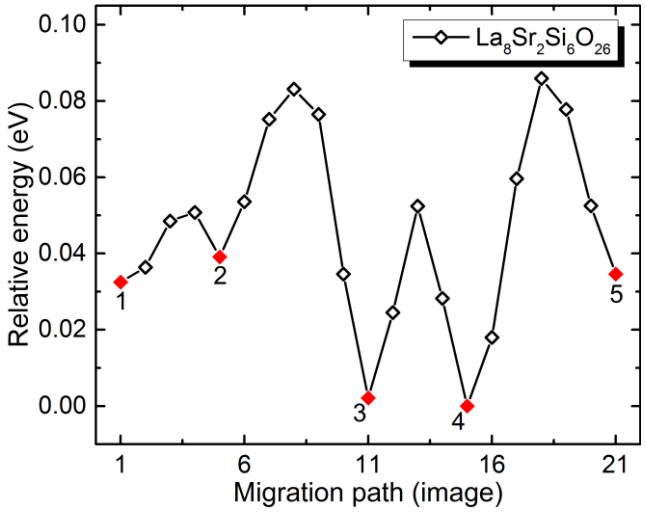

Figure 8 Energy profile of the interstitialcy migration in $La_8Sr_2Si_6O_{26}$ along the *c*-axis. The solid red symbols show stable configurations. The hollow black symbols represent NEB images. The numeration of the stable configurations corresponds with Figure 7. The line provides a guide to the eye.

Matsunaga *et al.* and Imaizumi *et al.* showed that the consideration of migration in the *ab* plane is also necessary for $La_{9.33}Si_6O_{26}$ and $La_{10}Si_6O_{27}$.[11,12] Their calculated migration energies in the *ab* direction for these compositions are 0.38 eV ($La_{9.33}Si_6O_{26}$) and 0.61 eV ($La_{10}Si_6O_{27}$), which are significantly higher than in the *c* direction and thus increase the overall activation energy. For comparison, we calculated the migration path between two oxygen channels in $La_8Sr_2Si_6O_{26}$. Three oxygen ions are involved in the migration and are tracked using different colours in Figure 9; Figure 10 shows the corresponding energy profile for two different paths. The orange interstitial starts from an O5 interstitial site of layer I (configuration 1) and migrates out of the tunnel towards an adjacent SiO_4 tetrahedron. The tetrahedron reorients and forms a pyramidal SiO_5 polyhedron with the interstitial (configuration 2). In a second step, the oxygen ion closest to the adjacent tetrahedron (yellow) moves to form a new SiO_5 polyhedron (configuration 3) while the original polyhedron relaxes to its original tetrahedral shape. Subsequently, the oxygen ion closest to the next La-tunnel (pink) moves away from the polyhedron and migrates to an O5 interstitial site of layer II inside the La-tunnel (configuration 4). Between configuration 2 and 3, the oxygen ion migrates past two 4f sites that are either occupied by La (La-edge) or Sr (Sr-edge) which alter the energy profile of the whole migration. For $La_8Sr_2Si_6O_{26}$ the energy barrier for *ab* migration is 0.52 eV along the La-edge (black curve) and 0.49 eV along the Sr-edge (blue curve), as depicted in Figure 10. The data suggests that doping the migration edge with Sr has little effect on the energy profile of the *ab* migration. The energy barriers for the oxygen ion to leave and enter the La-tunnel are similar, as expected (configuration 1→2 and 3→4). The polyhedron conformation in configuration 2 and 3, appear to be energetically equivalent due to an identical cation vicinity. However, different orientations of SiO_5 polyhedra towards the cation vicinity exist; therefore, the particular distances between the oxygen ions of the polyhedron and the adjacent La/Sr ions determine the configuration energies (configurations 2 and 3) and the transition energy (cf. Figure S8). Nevertheless, the migration energy is in agreement with the calculations by Imaizumi *et al.* and suggests the importance of the *ab* migration for the oxygen ion conductivity.[12]

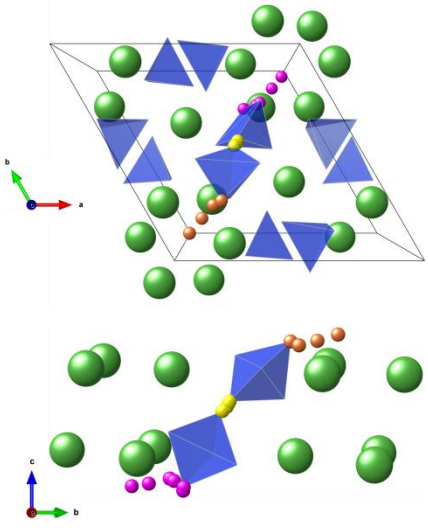

Figure 9 Interstitialcy migration of oxygen ions in the *ab* plane from one La-tunnel to an adjacent La-tunnel viewed along the *c*-axis (top) and from the *ab* plane (bottom). Each colour tracks one oxygen ion. The orange interstitial ion migrates out of the La-tunnel and forms a SiO_5 polyhedron. The polyhedron relaxes and forms a pyramid. The oxygen ion on the angle closest to the proximate tetrahedron (yellow) migrates there, forming a pyramidal SiO_5. Based on the arrangement of the polyhedron, the oxygen ion closest to the adjacent La-tunnel (pink) migrates into the tunnel.

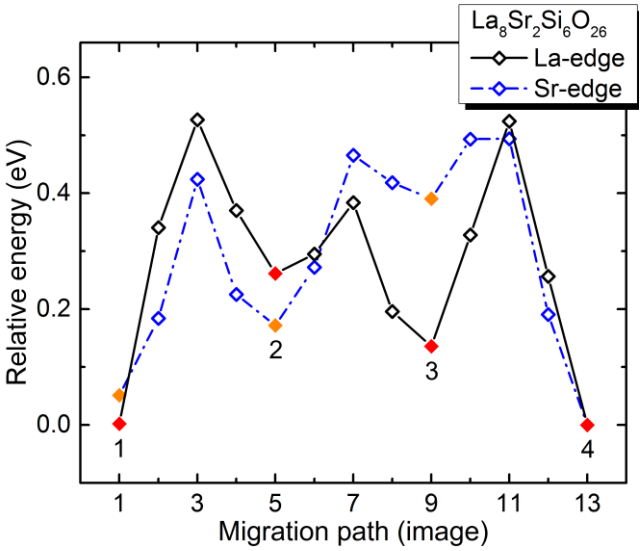

Figure 10 Energy profile of the interstitialcy migration in $La_8Sr_2Si_6O_{26}$ in the *ab* plane. The solid symbols show stable configurations. The hollow symbols show interpolated NEB images. The oxygen ion migrates past two 4f sites both occupied by either La (La-edge) or Sr (Sr-edge). The line provides a guide to the eye.

$La_{10}Si_6O_{27}$

In $La_{10}Si_6O_{27}$ the 4f sites are occupied entirely by La ions and the excess positive charge is compensated by one oxygen ion interstitial per formula unit. In a 1x1x3 supercell, three oxygen ion interstitials are present in the structure and expected to be located inside the La-tunnel. The migration in $La_{9.33}Si_6O_{26}$ and $La_8B_2Si_6O_{26}$ already demonstrated the little space in the La-tunnel as well as how the repulsion of the oxygen ions leads to an interstitialcy migration mechanism. For $La_{10}Si_6O_{27}$ the oxygen ion interstitials are no longer diluted, and the repulsive interactions increase. Imaizumi *et al.* report the same effect using the PBE XC functional, which leads to larger cell volumes compared to PBEsol (Table S1). To lower the repulsive interaction, oxygen ions tend to migrate out of the La-tunnel to an adjacent SiO_4 tetrahedron, forming a SiO_5 polyhedron. Therefore, we created supercells with different allocations of oxygen interstitials inside the La-tunnel and outside at SiO_5 polyhedra. The stability of the supercell increased with decreasing interstitial concentration inside the La-tunnel. Thus, further calculations were conducted on a supercell with one migrating interstitial located inside the tunnel and two interstitials located in SiO_5 polyhedra outside the tunnel. This way, the population of the remaining interstitials inside the La-tunnel was depleted and the repulsion decreased. The calculations showed that the bottleneck for oxygen ion migration is the migration of O5 interstitials past the SiO_5 polyhedra in an otherwise analogous migration pattern to the compositions outlined above. Figure 11 shows this determining step of the migration for one arrangement of the interstitials with the SiO_5 polyhedra rotated 180° around the *c*-axis. Each colour tracks one oxygen ion from configuration 5 to 6. The oxygen interstitials immobilized at the SiO_5 are depicted in pink. Due to little available space and a high local concentration of interstitials inside the tunnel and at the adjacent SiO_5 polyhedra, a strong interaction forces three oxygen ions to adapt to the interstitial motion, while, in the absence of SiO_5 polyhedra, only two oxygen ions are involved in the migration mechanism at most. Figure 12 shows the corresponding energy profile of the migration. The described bottleneck is the migration between configuration 5 and 6. The total height of the energy profile from configuration 1 to the maximum found by CI NEB is 0.62 eV, which is the highest total energy barrier for interstitial migration in the *c* direction for all considered compositions. The highest individual energy barrier is 0.31 eV and is attributed to the transition of configuration 5 to 6 described above. The migration barriers are similar to that of $La_{9.33}Si_6O_{26}$ but with an additional O5-O5 interaction.

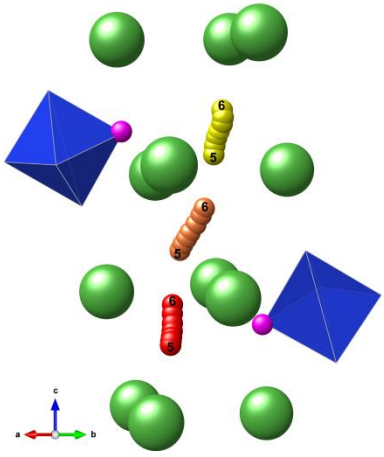

Figure 11 Migration path of O4/O5 oxygen ions in $La_{10}Si_6O_{27}$ along the c-axis between configuration 5 and 6 past the SiO_5 polyhedra. Each colour tracks one oxygen ion. The pink oxygen ions show the static interstitials at the SiO_5 polyhedra.

Discussion

The obtained migration energies of 1.22 eV to 2.00 eV (Table 1) for the vacancy mechanism in $La_8B_2Si_6O_{26}$ agree with experimental data for B = Ca, Sr, Ba (1.14 eV to 1.62 eV), while ionic conductivities for $La_8Mg_2Si_6O_{26}$ have not been reported so far.[33] The close agreement proves that the vacancy mechanism is the determining migration mechanism for these compositions. The presence of oxygen vacancies could be due to a deviation in the synthesis composition; for example, a small excess of B cations can be balanced by oxygen vacancies. In contrast, the intrinsic formation of vacancies is unlikely due to the high energy for anti-Frenkel disorder (Table S1). In addition, in the case of intrinsic disorder, the energy of formation would contribute to the measured activation energy ($E_A = 0.5 \cdot \Delta E_{aF} + E_{mig}$) leading to very high values of E_A.

The vacancy mechanism cannot explain the experimental results for $La_{9.33}Si_6O_{26}$ with activation energies between 0.4 eV and 1 eV. Therefore, the migration has to be described by the interstitialcy mechanism.[8] Analogous to the doped structures, a high anti-Frenkel energy excludes intrinsic formation as a major cause of defects and deviation in the synthesis composition is more likely,

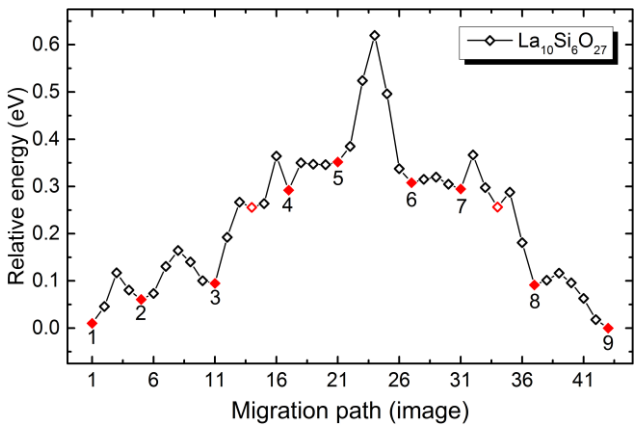

Figure 12 Energy profile of the interstitialcy migration in $La_{10}Si_6O_{27}$ along the *c*-axis. The solid symbols show stable configurations of energy minima. The hollow symbols show interpolated NEB images; hollow red symbols show intermediate minima found by CI NEB. The numeration of the stable configurations corresponds with those in Figure 11. The line provides a guide to the eye.

introducing oxygen interstitials with higher La content. For $La_{9.33}Si_6O_{26}$ the calculated migration barrier for the interstitialcy mechanism (0.30 eV) underestimates the majority of experimental data by half the value, while for the doped compounds, the barriers are even lower (0.09 eV – 0.18 eV). However, the calculated barriers agree with the results of previous theoretical studies.[10,11] It should be noted that the calculated energy barriers do not resemble the actual activation energies of these materials since only migration in the *c*-axis direction is considered, whereas in experimental measurements of polycrystalline samples where all directions contribute to the overall resistance and activation energy. Fukuda *et al.* reported activation energies on highly *c*-axis-oriented polycrystalline $La_{9.33}Si_6O_{26}$ and $La_{9.50}Si_6O_{26.25}$ of 0.35 eV for migration in the *c* direction, which agree with the present results.[14,15] Furthermore, they reported an activation energy of 0.71 eV for *ab* migration in the same materials which agrees with Nakayama *et al.*'s measurements on single crystalline $La_{9.33}Si_6O_{26}$. These measurements showed an activation energy of 0.68 eV in the *ab* plane and 0.65 eV along the *c*-axis.[36] Our calculations for $La_8Sr_2Si_6O_{26}$ show that the energy barrier for *ab* migration (0.52 eV) is approx. 5 times higher than the energy barrier for *c* migration (0.09 eV), but fits the range of the experimental data.

Even in single crystals, the migration might not occur solely in *c* direction, but effects like immobilized O5 oxygen ions at SiO_5 polyhedra, repulsion among interstitials and impurities might block the channels, enforcing migration in the *ab* plane. These effects could explain the similar activation energies for *c* and *ab* migration measured by Nakayama *et al.*. Imaizumi *et al.* came to the same conclusion for $La_{10}Si_6O_{27}$ and attributed the high activation energy (0.58 eV) to the potential barrier for the migration in and out of the La-tunnel.[12] In the present study, we calculated a migration energy of 0.62 eV for the interstitialcy mechanism in $La_{10}Si_6O_{27}$ which fits the experimental data of 0.47 eV to 0.72 eV.[34,37–40] In the calculated supercell two of three interstitials were placed on sites outside of the La-tunnel, which further suggests that the presence of SiO_5 polyhedra and their effect on migration along the *c*-axis in lanthanum apatite structures are not negligible.[12]

The oxygen ion conductivity is strongly dependent on the migration mechanism, which is defined by the deviation of the ideal oxygen content. Since the intrinsic formation of defects is unlikely, it is expected that the effective La stoichiometry of compositions in experimental publications may be different than stated.

Thus, both the vacancy and interstitialcy mechanisms are possible in $La_{9.33}Si_6O_{26}$ and $La_8B_2Si_6O_{26}$ depending on the non-stoichiometry of the oxygen content. For $La_{10}Si_6O_{27}$ only an interstitialcy mechanism is feasible. Nonetheless, only some possible cation/cation vacancy distributions have been considered to date and further compositions must be regarded in future to consolidate the obtained results.

Conclusion

We calculated the migration energies in lanthanum apatite structures with the composition $La_{9.33}Si_6O_{26}$, $La_{10}Si_6O_{27}$ and $La_8B_2Si_6O_{26}$ (*B* = Mg, Ca, Sr, Ba). In these structures, the oxygen ion can be transported by either the vacancy or interstitialcy mechanism. For both mechanisms, the Sr-doped composition $La_8Sr_2Si_6O_{26}$ shows a minimum in migration energy along *c* direction. While the computational results for the doped composition show good agreement with the literature with respect to the vacancy mechanism, this does not explain the high oxygen ion conductivities and low activation energies for higher La content. Furthermore, high anti-Frenkel formation energies exclude intrinsic disorder. Thus, the defect concentration is entirely dependent on the non-stoichiometry of the oxygen content due to synthesis conditions. We propose that the high oxygen ion conductivity and low activation energy in lanthanum apatites are attributed to an interstitialcy mechanism due to compensation of excessive La content by oxygen interstitials. In turn, we attribute a low oxygen ion conductivity and high activation energy to a vacancy mechanism as a consequence of an increased *B* content and compensating oxygen vacancies. $La_{9.33}Si_6O_{26}$ and $La_{10}Si_6O_{27}$ appear to follow only interstitialcy mechanisms. However, the calculated results underestimate most of the experimental data; only $La_{10}Si_6O_{27}$ matches comprehensively. Based on this, it is clear that effects like interstitialcy migration in the *ab* plane and immobilization of interstitials in SiO_5 polyhedra must be considered. Therefore, it is important to improve the migration mechanisms and combine the mechanisms for *c* and *ab* migration to acquire a comprehensive model. In addition, experimental data with confirmed compositions are essential to compare the theoretical data effectively.

ASSOCIATED CONTENT

Supporting Information

Figures S1 to S8 (structural illustration, energy profiles) and Table S1 (bulk volumes and anti-Frenkel energies). This material is available free of charge via the Internet at http://pubs.acs.org.

AUTHOR INFORMATION

Corresponding Author

* E-mail: s.grieshammer@fz-juelich.de

Author Contributions

The manuscript was written through contributions of all authors.

ACKNOWLEDGMENT

This research was funded by the German Research Foundation (DFG Grant no. GR-5011/1-1).

The authors gratefully acknowledge the computing time granted by the JARA-HPC Vergabegremium and provided on the JARA-HPC Partition part of the supercomputer CLAIX at RWTH Aachen University.

REFERENCES

(1) Steele, B. C. H.; Heinzel, A. Materials for Fuel-Cell Technologies. *Nature* **2001**, *414*, 345–352.

(2) Nakamura, A. Defect Structure, Ionic Conductivity, and Diffusion in Yttria Stabilized Zirconia and Related Oxide Electrolytes with Fluorite Structure. *J. Electrochem. Soc.* **1986**, *133*, 1542.

(3) León-Reina, L.; Losilla, E. R.; Martínez-Lara, M.; Bruque, S.; Aranda, M. A. G. Interstitial Oxygen Conduction in Lanthanum Oxy-Apatite Electrolytes. *J. Mater. Chem.* **2004**, *14*, 1142–1149.

(4) León-Reina, L.; Porras-Vázquez, J. M.; Losilla, E. R.; Aranda, M. A. G. Interstitial Oxide Positions in Oxygen-Excess Oxy-Apatites. *Solid State Ionics* **2006**, *177*, 1307–1315.

(5) Panchmatia, P. M.; Orera, A.; Rees, G. J.; Smith, M. E.; Hanna, J. V.; Slater, P. R.; Islam, M. S. Oxygen Defects and Novel Transport Mechanisms in Apatite Ionic Conductors: Combined ^{17}O NMR and Modeling Studies. *Angew. Chemie - Int. Ed.* **2011**, *50*, 9328–9333.

(6) Momma, K.; Izumi, F. VESTA 3 for Three-Dimensional Visualization of Crystal , Volumetric and Morphology Data. *J. Appl. Crystallogr.* **2011**, *44*, 1272–1276.

(7) Sansom, J. E. H.; Kendrick, E.; Tolchard, J. R.; Islam, M. S.; Slater, P. R. A Comparison of the Effect of Rare Earth vs Si Site Doping on the Conductivities of Apatite-Type Rare Earth Silicates. *J. Solid State Electrochem.* **2006**, *10*, 562–568.

(8) Kobayashi, K.; Sakka, Y. Research Progress in Nondoped Lanthanoid Silicate Oxyapatites as New Oxygen-Ion Conductors. *J. Ceram. Soc. Japan* **2014**, *122*, 921–939.

(9) Tolchard, J. R.; Islam, M. S.; Slater, P. R. Defect Chemistry and Oxygen Ion Migration in the Apatite-Type Materials $La_{9.33}Si_6O_{26}$ and $La_8Sr_2Si_6O_{26}$. *J. Mater. Chem.* **2003**, *13*, 1956.

(10) Béchade, E.; Masson, O.; Iwata, T.; Julien, I.; Fukuda, K.; Thomas, P.; Champion, E. Diffusion Path and Conduction Mechanism of Oxide Ions in Apatite-Type Lanthanum Silicates. *Chem. Mater.* **2009**, *21*, 2508–2517.

(11) Matsunaga, K.; Toyoura, K. First-Principles Analysis of Oxide-Ion Conduction Mechanism in Lanthanum Silicate. *J. Mater. Chem.* **2012**, *22*, 7265.

(12) Imaizumi, K.; Toyoura, K.; Nakamura, A.; Matsunaga, K. Strong Correlation in 1D Oxygen-Ion Conduction of Apatite-Type Lanthanum Silicate. *J. Phys. Condens. Matter* **2015**, *27*, 365601.

(13) Nakayama, S.; Ikesue, A.; Higuchi, Y.; Sugawara, M.; Sakamoto, M. Growth of Single-Crystals of Apatite-Type Oxide Ionic Conductor from Sintered Ceramics by a Seeding Method. *J. Eur. Ceram. Soc.* **2013**, *33*, 207–210.

(14) Fukuda, K.; Asaka, T.; Okino, M.; Berghout, A.; Béchade, E.; Masson, O.; Julien, I.; Thomas, P. Anisotropy of Oxide-Ion Conduction in Apatite-Type Lanthanum Silicate. *Solid State Ionics* **2012**, *217*, 40–45.

(15) Fukuda, K.; Asaka, T.; Oyabu, M.; Urushihara, D.; Berghout, A.; Béchade, E.; Masson, O.; Julien, I.; Thomas, P. Crystal Structure and Oxide-Ion Conductivity along *c* -Axis of Apatite-Type Lanthanum Silicate with Excess Oxide Ions. *Chem. Mater.* **2012**, *24*, 4623–4631.

(16) Kresse, G.; Hafner, J. Ab Initio Molecular Dynamics for Liquid Metals. *Phys. Rev. B* **1993**, *47*, 558–561.

(17) Kresse, G.; Hafner, J. Ab Initio Molecular-Dynamics Simulation of the Liquid-Metal–amorphous-Semiconductor Transition in Germanium. *Phys. Rev. B* **1994**, *49*, 14251–14269.

(18) Kresse, G.; Furthmüller, J. Efficiency of Ab-Initio Total Energy Calculations for Metals and Semiconductors Using a Plane-Wave Basis Set. *Comput. Mater. Sci.* **1996**, *6*, 15–50.

(19) Kresse, G.; Furthmüller, J. Efficient Iterative Schemes for Ab Initio Total-Energy Calculations Using a Plane-Wave Basis Set. *Phys. Rev. B* **1996**, *54*, 11169–11186.

(20) Blöchl, P. E. Projector Augmented-Wave Method. *Phys. Rev. B* **1994**, *50*, 17953–17979.

(21) Kresse, G.; Joubert, D. From Ultrasoft Pseudopotentials to the Projector Augmented-Wave Method. *Phys. Rev. B* **1999**, *59*, 1758–1775.

(22) Perdew, J. P.; Burke, K.; Ernzerhof, M. Generalized Gradient Approximation Made Simple. *Phys. Rev. Lett.* **1996**, *77*, 3865–3868.

(23) Perdew, J. P.; Burke, K.; Ernzerhof, M. Generalized Gradient Approximation Made Simple- ERRATA. *Phys. Rev. Lett.* **1996**, *77*, 3865–3868.

(24) Perdew, J.; Ruzsinszky, A.; Csonka, G.; Vydrov, O.; Scuseria, G.; Constantin, L.; Zhou, X.; Burke, K. Restoring the Density-Gradient Expansion for Exchange in Solids and Surfaces. *Phys. Rev. Lett.* **2008**, *100*, 136406.

(25) Iwata, T.; Fukuda, K.; Béchade, E.; Masson, O.; Julien, I.; Champion, E.; Thomas, P. Structural Change of Oxide-Ion-Conducting Lanthanum Silicate on Heating from 295 to 1073 K. *Solid State Ionics* **2007**, *178*, 1523–1529.

(26) Borg, S.; Svensson, G. Crystal Structure of $Bi_{2.5}Me_{0.5}Nb_2O_9$ (Me= Na, K): A Powder Neutron Diffraction Study. *J. Solid State Chem.* **2001**, *157*, 160–165.

(27) Matsushita, Y.; Izumi, F.; Kobayashi, K.; Igawa, N.; Kitazawa, H.; Oyama, Y.; Miyoshi, S.; Yamaguchi, S. Powder Neutron Diffraction of La-Apatite under Low Temperature. *Nucl. Instruments Methods Phys. Res. Sect. A Accel. Spectrometers, Detect. Assoc. Equip.* **2009**, *600*, 319–321.

(28) Sheppard, D.; Terrell, R.; Henkelman, G. Optimization Methods for Finding Minimum Energy Paths. *J. Chem. Phys.* **2008**, *128*.

(29) Sheppard, D.; Xiao, P.; Chemelewski, W.; Johnson, D. D.; Henkelman, G. A Generalized Solid-State Nudged Elastic Band Method. *J. Chem. Phys.* **2012**, *136*.

(30) Sheppard, D.; Henkelman, G. Paths to Which the Nudged Elastic Band Converges. *J. Comput. Chem.* **2011**, *32*, 1769–1771.

(31) Henkelman, G.; Jónsson, H. Improved Tangent Estimate in the Nudged Elastic Band Method for Finding Minimum Energy Paths and Saddle Points. *J. Chem. Phys.* **2000**, *113*, 9978–9985.

(32) Henkelman, G.; Uberuaga, B. P.; Jónsson, H. Climbing Image Nudged Elastic Band Method for Finding Saddle Points and Minimum Energy Paths. *J. Chem. Phys.* **2000**, *113*, 9901–9904.

(33) Slater, P. R.; Sansom, J. E. H. The Synthesis and Characterisation of New Apatite-Type Oxide Ion Conductors. *Solid State Chem. V* **2003**, *90–91*, 195–200.

(34) Nakayama, S.; Sakamoto, M. Electrical Properties of New Type High Oxide Ionic Conductor $RE_{10}Si_6O_{27}$ (RE = La, Pr, Nd, Sm, Gd, Dy). *J. Eur. Ceram. Soc.* **1998**, *18*, 1413–1418.

(35) Koettgen, J.; Grieshammer, S.; Hein, P.; Grope, B. O. H.; Nakayama, M.; Martin, M. Understanding the Ionic Conductivity Maximum in Doped Ceria: Trapping and Blocking. *Phys. Chem. Chem. Phys.* **2018**, *20*, 14291–14321.

(36) Nakayama, S.; Sakamoto, M. Preparation of Apatite-Type $La_{9.33}Ge_6O_{26}$ Single-Crystal from Sintered Ceramics by a Seeding Method and Its Oxide Ionic Conduction. *Solid State Ionics* **2013**, *253*, 47–52.

(37) Nakayama, S.; Kageyama, T.; Aono, H.; Sadaoka, Y. Ionic Conductivity of Lanthanoid Silicates, $Ln_{10}(SiO_4)_6O_3$ (Ln = La, Nd, Sm, Gd, Dy, Y, Ho, Er and Yb). *J. Mater. Chem.* **1995**, *5*, 1801–1805.

(38) Yoshioka, H.; Nojiri, Y.; Tanase, S. Ionic Conductivity and Fuel Cell Properties of Apatite-Type Lanthanum Silicates Doped with Mg and Containing Excess Oxide Ions. *Solid State Ionics* **2008**, *179*, 2165–2169.

(39) Nojiri, Y.; Tanase, S.; Iwasa, M.; Yoshioka, H.; Matsumura, Y.; Sakai, T. Ionic Conductivity of Apatite-Type Solid Electrolyte Material, $La_{10-X}Ba_XSi_6O_{27-X/2}$ (X = 0-1), and Its Fuel Cell Performance. *J. Power Sources* **2010**, *195*, 4059–4064.

(40) Arikawa, H.; Nishiguchi, H.; Ishihara, T.; Takita, Y. Oxide Ion Conductivity in Sr-Doped $La_{10}Ge_6O_{27}$ Apatite Oxide.

Solid State Ionics **2000**, *136–137*, 31–37.